Multi-Sensor Terrain Estimation for Planetary Rovers

Karl Iagnemma, Shinwoo Kang, Christopher Brooks, Steven Dubowsky
Massachusetts Institute of Technology
Room 3-435A, 77 Massachusetts Avenue, Cambridge, MA, 02139 USA
{kdi,ksw,cabrooks,dubowsky}@mit.edu

Keywords Rovers, Planetary Exploration, Rough Terrain, Sensing

Abstract

Future planetary exploration missions will require rovers to perform difficult tasks in rough terrain, with limited human supervision. Knowledge of terrain physical characteristics would allow a rover to adapt its control and planning strategies to maximize its effectiveness. This paper describes recent and current work at MIT in the area of terrain estimation and sensing. A method for on-line terrain parameter estimation is presented. A complementary method for terrain traversability estimation is also presented. Sensor issues related to terrain estimation are discussed, and a vision-based method for measuring wheel sinkage is described. It is shown that these methods can lead to accurate and efficient understanding of a rover's physical surroundings.

1. Introduction

Future planetary exploration missions will require rovers to perform challenging mobility tasks in rough terrain [8]. Wheel-terrain interaction has been shown to play a critical role in rough-terrain mobility [1]. For example, a rover traveling through loose drift material has very different mobility characteristics than one traveling over hard, crusty terrain.

For planetary rovers, it would be desirable to gather on-line information about the surrounding terrain. This can be done by estimating terrain physical parameters (e.g. cohesion, internal friction angle, shear deformation modulus, etc.) or estimating some metric of terrain traversability. Knowledge of terrain characteristics would allow a rover to adapt its control and planning strategy to optimize its performance, such as maximizing traction or minimizing power consumption [2, 3]. Also, terrain parameter estimation can improve scientific understanding of planetary surface composition [5].

This paper describes recent and current work in the Field and Space Robotics Laboratory at MIT in algorithm development for terrain estimation and sensing [4]. A terrain parameter estimation algorithm is presented that relies on a simplified form of classical terramechanics equations, and uses a linear-least squares estimator to compute terrain parameters in real time. The method is computationally efficient, and is thus suitable for implementation on a rover with limited on-board computational resources. Simulation and experimental results show that the algorithm can accurately and efficiently identify key terrain parameters for a variety of soil types.

A new method for terrain traversability estimation is also presented that uses data from on-board sensors and model-based analysis to predict traversability. Here, the rover "feels" the terrain, and correlates wheel torque and sinkage with an on-board database of predicted drawbar pull (i.e. net wheel thrust, minus motion resistance) [1]. Drawbar pull is an indicator of a rover's ability to move through terrain. This technique is complementary to the parameter estimation method described above. Simulation results are presented that demonstrate the effectiveness of this technique.

An important practical aspect of terrain estimation is sensing. Wheel torque, load, and sinkage are inputs to terrain estimation algorithms. Methods for sensing these quantities are discussed. A simple vision-based

method for measuring wheel sinkage is described. Experimental results are presented for wheel sinkage estimation under various conditions.

It is shown that these methods can lead to accurate and efficient understanding of a rover's physical surroundings. Such techniques could enhance rover safety and mobility, through integration with control and motion planning methods.

2. Multi-Sensor Terrain Estimation

For planetary rovers, it would be desirable to estimate terrain characteristics on-line. This can be done by estimating terrain physical parameters (e.g. cohesion, internal friction angle, shear deformation modulus, etc.) or estimating some metric of terrain traversability. Here, two methods for on-line estimation of terrain characteristics are presented.

2.1 Terrain Parameter Estimation

The case of a smooth rigid wheel traveling through deformable terrain is considered, as this is the expected condition for planetary exploration vehicles (see Figure 1). A more detailed treatment of this method is presented in [4]. Note that the following analysis also applies to grousered wheels, since grousers can be modeled by increasing the effective wheel radius [10].

To estimate terrain parameters, equations relating the parameters of interest to physically measurable quantities must be developed. The physical parameters of interest are the terrain cohesion c and the internal friction angle f. These parameters can be used to compute the maximum terrain shear strength, t_{max}, from Coulomb's equation:

$$t_{\max} = c + s_{\max} \tan f \qquad (1)$$

where s_{max} is the maximum normal stress acting on a terrain region.

In Figure 1, a vertical load W and drawbar pull DP are applied to the wheel by the vehicle suspension. A torque T is applied at the wheel rotation axis by an actuator. The wheel has angular velocity w, and the wheel center possesses a linear velocity, V. The angle from the vertical at which the wheel first makes contact with the terrain is denoted q_1. The angle from the vertical at which the wheel loses contact with the terrain is denoted q_2.

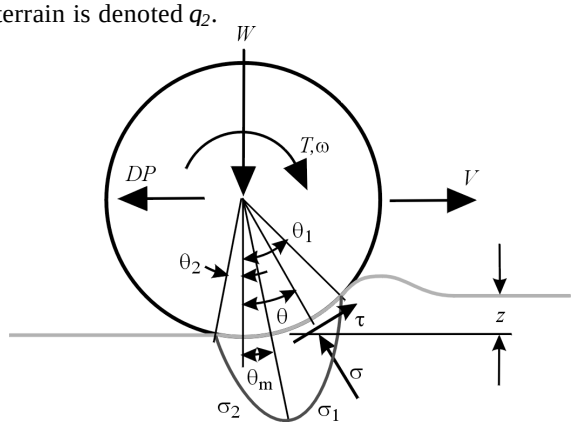

Figure 1: Rigid wheel on deformable terrain

A stress region is created at the wheel-terrain interface, and is indicated by s_1 and s_2. The angle from the vertical at which the maximum stress occurs is denoted q_m.

From Figure 1, force balance equations can be written as:

$$W = rb\left(\int_{q_2}^{q_1} s(q)\cos q \cdot dq + \int_{q_2}^{q_1} t(q)\sin q \cdot dq\right) \qquad (2)$$

$$DP = rb\left(\int_{q_2}^{q_1} t(q)\cos q \cdot dq - \int_{q_2}^{q_1} s(q)\sin q \cdot dq\right) \qquad (3)$$

$$T = r^2 b\int_{q_2}^{q_1} t(q)\cdot dq \qquad (4)$$

The shear stress can be computed as:

$$t(q) = (c + s(q)\tan f)\left(1 - e^{-\frac{r}{k}[q_1 - q - (1-i)(\sin q_1 - \sin q)]}\right) \qquad (5)$$

where k is the shear deformation modulus, r is the wheel radius, and i is the wheel slip, defined as $i = 1 - (V/rw)$ [9].

The normal stress at the wheel-terrain interface is given by:

$$s(z) = \left(\frac{k_c}{b} + k_f\right) z^n \qquad (6)$$

where b is the wheel width, k_1 and k_2 are pressure sinkage moduli, and n is the sinkage exponent [9].

Note that the shear and normal stress are functions of c and f, among other variables. Analytical solutions of Equations (2-4) are required to obtain closed-form expressions for c and f. However, the

complexity of these equations motivates the use of an approximate form of the fundamental stress equations.

Figure 2 is a plot of the shear and normal stress distributions around the rim of a driven rigid wheel on various deformable terrains. The shear and normal stress distribution curves are approximately triangular for a wide range of terrain.

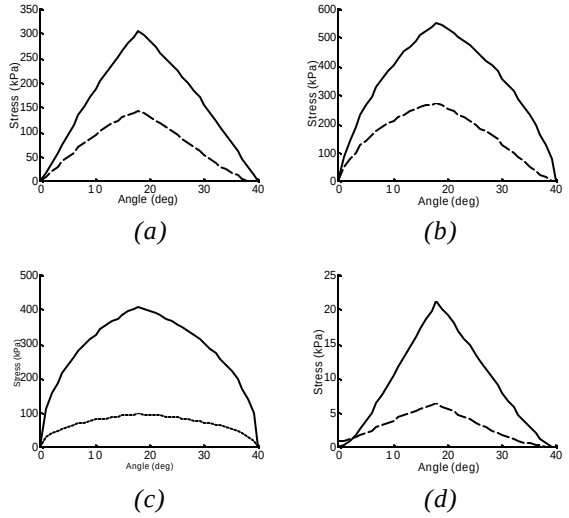

Figure 2: Normal (solid) and shear stress (dotted) distribution around driven rigid wheel for (a) dry sand, (b) sandy loam, (c) clayey soil, and (d) snow at moderate wheel slip [6, 9]

Based on this observation, a linear approximation of the shear and normal stress distribution equations can be written as:

$$s_1^L(q) = \frac{q_1 - q}{q_1 - q_m} s_m \tag{7}$$

$$s_2^L(q) = \frac{q}{q_m} s_m \tag{8}$$

$$t_1^L(q) = \frac{q_1 - q}{q_1 - q_m} t_m \tag{9}$$

$$t_2^L(q) = c + \frac{q}{q_m}(t_m - c) \tag{10}$$

Simplified forms of the force balance equations can be written and solved for the load W and torque T:

$$W = \frac{rb}{q_m(q_1 - q_m)} \begin{bmatrix} s_m(-q_m \cos q_1 + q_1 \cos q_m - q_1 + q_m) \\ -t_m(q_m \sin q_1 - q_1 \sin q_m) \\ -c(q_1 \sin q_m - q_m \sin q_m - q_m q_1 + q_m^2) \end{bmatrix} \tag{11}$$

$$T = \frac{r^2 b}{2}(t_m q_1 + c q_m) \tag{12}$$

An additional equation can be written if the location of the maximum shear and normal stress are assumed to occur at the same location q_m:

$$t_m = (c + s_m \tan f)\left(1 - e^{-\frac{r}{k}[q_1 - q_m - (1-i)(\sin q_1 - \sin q_m)]}\right) \tag{13}$$

The simplified equations can be solved for the cohesion and internal shear angle and rearranged in the following form (after additional simplification):

$$\frac{k_2}{k_3} = c + \frac{k_1}{k_3} \tan f \tag{14}$$

where

$$k_1 = A\left(q_1^2 Wr + 4T \sin q_1 - 8T \sin \frac{q_1}{2}\right)$$

$$k_2 = 4T\left(\cos q_1 - 2\cos \frac{q_1}{2} + 1\right)$$

$$k_3 = q_1 r^2 b \begin{pmatrix} \cos q_1 - 2\cos \frac{q_1}{2} + 2A\cos q_1 \\ -4A\cos \frac{q_1}{2} + 2A + 1 \end{pmatrix}$$

and $A = 1 - e^{-\frac{r}{k}\left[\frac{q_1}{2} + (1-i)\left(-\sin q_1 + \sin\left(\frac{q_1}{2}\right)\right)\right]}$.

Equation (14) is a single equation in two unknowns. At least two unique instances of Equation (14) are required to determine c and f. In practice numerous unique instances of Equation (14) can be written as a rover moves through terrain. Least-squares techniques can then be used to solve for c and f.

Figure 3 shows representative results of parameter estimation simulation for dry, sandy soil. It can be seen that the estimated parameters c and f quickly converge to the true values of c = 2.5 and f = 27.0.

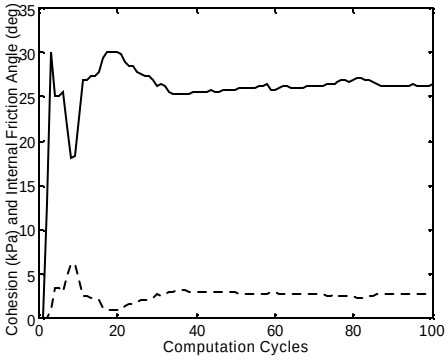

Figure 3: Simulated estimation of cohesion (dotted) and internal friction angle (solid)

Figure 4 shows experimental results of parameter

estimation of dried bentonite clay performed on a wheel-terrain interaction testbed (see Figure 5). Again, it can be seen that c and f quickly approach the measured values of c = 0.7 and f = 32.1.

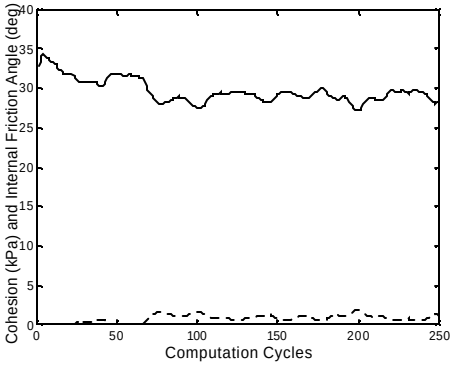

Figure 4: Experimental estimation of cohesion (dotted) and internal friction angle (solid)

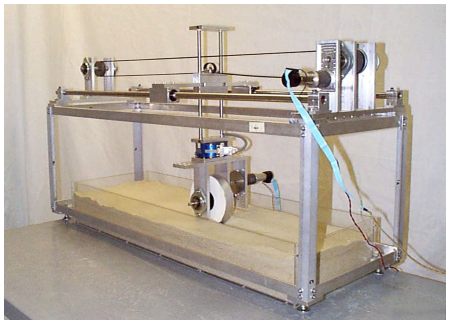

Figure 5: Wheel-terrain interaction testbed

These results show that the algorithm produces accurate, on-line parameter estimates on an experimental system with noisy sensors. The algorithm takes only a few msec per estimation cycle on a desktop PC, thus making it feasible for on-board implementation on a rover with limited computational resources.

Terrain parameter estimates from this algorithm can be used to optimize a rover's mobility and safety, and are themselves useful scientific information.

2.2 Non-Parametric Traversability Prediction

A complementary approach to understanding terrain physical properties is through non-parametric traversability prediction. Here, the goal is not to estimate specific terrain parameters, but rather to predict rover traversability. This knowledge could be in control and motion planning algorithms to improve rover safety and mobility.

Drawbar pull was chosen as the mobility index. Drawbar pull can be used to assess traversability across flat and uneven terrain. However, direct measurement of drawbar pull is difficult since there is no fixed reference from which to measure forces.

Here we propose a method for estimating drawbar pull based on simple sensor measurements. The rover "feels" the terrain by driving a single wheel and measuring the torque and sinkage. Other rover wheels are either fixed or moving at a constant angular velocity during this process. The torque and sinkage are then correlated with an on-board database of predicted drawbar pull. This yields an estimate of the local terrain mobility.

This method was inspired by empirical observations between torque, sinkage, and drawbar pull. It was observed that terrain with low wheel sinkage and high torque, such as hardpack or pavement, generally allows large drawbar pull. Terrain with high sinkage and low torque, such as sand or dust, generally allows low drawbar pull. This implies that knowledge of sinkage and torque are important indicators of drawbar pull. These observations is exploited in the traversability prediction method.

Figure 6 expresses these observations as a heuristic mapping from torque and sinkage to drawbar pull. Here the torque T and sinkage z have been nondimensionalized by wheel radius r and weight W. The torque T refers to the maximum torque applied to a terrain region at a given level of slip.

T/rW \ z/r	0.1	0.2	0.3
0.7	Good	Good	Med
0.5	Med	Med	Med
0.3	Med	Poor	Poor

Figure 6. Empirical correlation of drawbar pull level to sinkage and torque for various terrain classes

Simulations were conducted to examine the validity of this approach. Equations (2-6) were used to

determine the drawbar pull generated by a rigid wheel under a variety of different terrain conditions. Table 1 lists six different terrain classes used in the simulations. These classes represent unique terrain types, such as sandy soil, clayey soil, hard soil, etc. Various combinations of parameters within each terrain class were simulated. In these simulations the wheel radius was 0.15 m, wheel width was 0.1 m, the slip ratio ranged from 0.2-0.9, and the vertical wheel load W ranged from 30-90 N. The shear deformation modulus K ranged from 0.01-0.03 m, and the sinkage exponent n ranged from 0.5-1.2.

Table 1: Terrain classes for drawbar pull simulation

Terrain Class	Hardness ($k_c/b+K_f$) (kPa)	Cohesion (kPa)	Internal Friction Angle (°)
1	500~1500	8~12	5~15
2	500~1500	0~1	20~30
3	1000~3000	0~1	30~45
4	1000~3000	2~5	20~30
5	1000~3000	8~12	20~30
6	3000~6000	2~5	30~45

A representative result of these simulations is shown in Figure 7. This figure shows drawbar pull versus nondimensionalized torque and sinkage (the vertical axis of each subplot is the nondimensionalized drawbar pull, DP/W). The axes have been divided in three regions for ease of viewing. The small variation in the simulation data indicates that sinkage and torque are good indicators of drawbar pull, independent of explicit knowledge of terrain parameters.

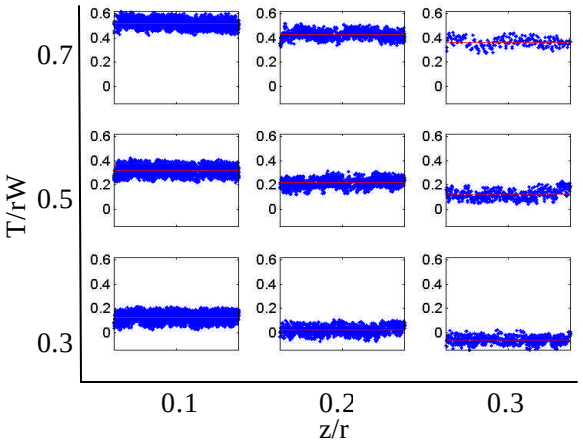

Figure 7. Drawbar pull vs. sinkage and torque for various terrain classes

Mobility prediction can be performed based on the mean and deviation of data in given grouping. For example, in Figure 7 a z/r value near 0.3 and a T/rW value near 0.3 implies a mean drawbar pull prediction of 0.02 with standard deviation of 0.03. Though the predicted drawbar pull is positive, the data variation implies that this prediction contains significant uncertainty. In contrast, a z/r value of 0.1 and a T/rW value of 0.7 implies a mean drawbar pull prediction of 0.5 with standard deviation of 0.03. The high drawbar pull and low data variation implies that this terrain is safely traversable.

It is envisioned that the traversability estimation algorithm would be employed as follows:

1) Before rover flight or deployment, a database similar to Figure 7 would be constructed (through simulation) over a wide variety of terrain conditions, for a nominal wheel load. Note that a best-fit analytical mapping from z/r and T/rW to expected DP can easily be constructed, reducing on-board memory requirements.

2) When unknown terrain is encountered, the rover would perform a single-wheel trenching experiment, simultaneously collecting wheel slip, torque, and sinkage data. The maximum torque and sinkage would be extracted from this data.

3) Wheel torque and sinkage would be used to predict terrain traversability. The rover would modify its control or motion plan accordingly. Note that traversability estimates could be correlated with distant terrain through matching of geometric, color, textural, or multispectral cues. This is an area of current research.

Figure 8 shows experimental results of traversability estimation of dried bentonite clay using the wheel-terrain interaction testbed. In these experiments, slip, torque, and sinkage were measured under a known wheel weight, and DP/W was predicted using the method described above. It can be seen that the difference between the measured and predicted DP/W is small, implying that the proposed method can predict traversability with reasonable accuracy. In this particular result, the terrain exhibits very poor

traversability.

Further experimental validation of this approach is currently being conducted on a variety of soil types.

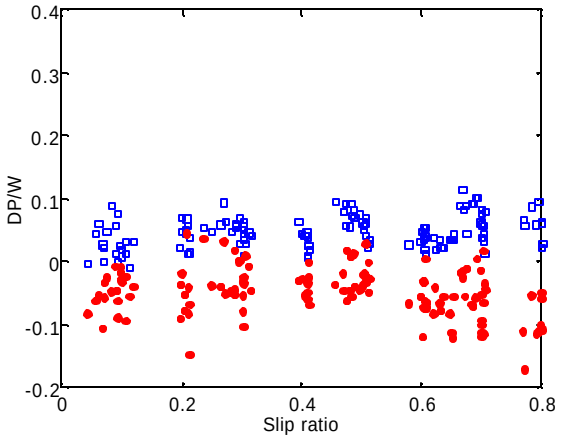

Figure 8. Predicted (solid) and experimentally measured (hollow) drawbar pull vs. slip ratio for dried bentonite clay

3. Sensing Issues

To perform multi-sensor terrain estimation, the wheel load, torque, slip, and sinkage must be measured or estimated.

Wheel load can be computed from a quasi-static force analysis of the rover, with knowledge of the rover configuration and mass distribution. A quasi-static analysis is valid since dynamic effects are negligible due to the low speeds of these vehicles (i.e. on the order of 10 cm/sec).

Wheel torque can be estimated with reasonable accuracy from the current input to the motor and an empirically-determined mapping from current to torque. In applications where large thermal variation is expected (such as Martian surface exploration), the motor temperature could be included in this mapping for increased accuracy [5]. Note that the torque and vertical load could be directly measured if the wheel were instrumented with a multi-axis force sensor. However, this adds cost and complexity.

Wheel angular speed can be measured with a tachometer, and the linear speed can be computed using IMU measurements or visual odometry techniques [7]. These quantities are combined to compute wheel slip.

Wheel sinkage can be computed using a simple vision-based technique discussed below.

3.1 Visual Wheel Sinkage Estimation

Here, wheel sinkage is estimated visually using a body-mounted rover camera (see Figure 9). Such cameras have been integrated into JPL research rovers such as FIDO for underbelly hazard avoidance.

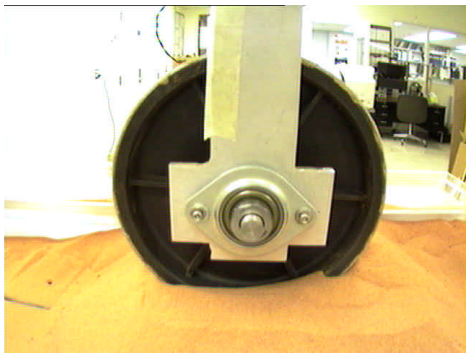

Figure 9. Example of wheel sinkage in terrain

It is assumed that the wheel rim is visually distinct from the surrounding soil. This can be accomplished by marking or coloring the wheel rim. This simplifies image segmentation and reduces computation time. Computational simplicity was a major consideration in algorithm development, as flight rovers will have limited processor time to devote to wheel sinkage computations.

The algorithm goal is to determine the wheel/terrain interface location, here defined as two angles from the vertical termed the terrain "entry" and "exit" angles (see Figure 10). This represents a general description of wheel sinkage on uneven terrain. Note that to determine these angles an annular region along the wheel rim is the only image area that needs to be examined. This reduces computational requirements by eliminating much of the scene.

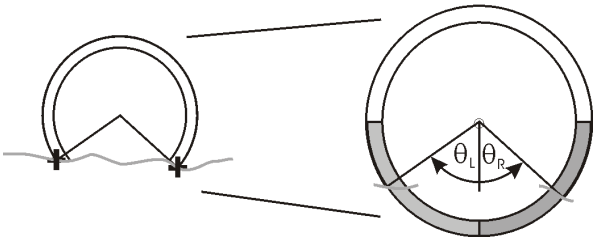

Figure 10. Sunken wheel with entry and exit angles marked and annular region shaded

The algorithm consists of the following steps:

1) Identifying the wheel rim annulus in the camera field of view. Here we assume that the position of the wheel center relative to the camera is known from suspension configuration sensors. Thus, computation of the wheel rim region involves simple geometric projection.

2) Dividing the annular region into left- and right-hand sections (see Figure 10). It is assumed that the left-hand section will contain the wheel-terrain "entry," and the right-hand section will contain the "exit" (i.e. a single wheel-terrain interface is present in each region). These regions will be treated separately in the following steps.

3) Computing average intensity (brightness) of pixels along horizontal rows in each region (i.e. rows perpendicular to the gravity vector). For a single-channel image, the average pixel intensity of each horizontal row is placed in a 1 x N array, where N is a function of the camera resolution. Thus, the left- and right-hand arrays describe the image intensity as a function of vertical position on the wheel.

4) Filtering both arrays to reduce noise and minimize small-scale changes in intensity caused by reflection, pebbles, etc. A representative plot of a filtered intensity array is shown in Figure 11. The intensity is low in the region where the black wheel rim is not obscured by terrain. The intensity is high where the sand is covering the wheel.

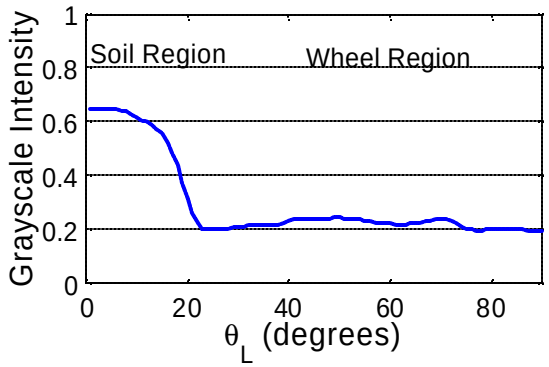

Figure 11. Plot of average pixel intensity vs. wheel angular position

5) Computing the wheel-terrain interface location as the point of maximum change in image intensity. In Figure 11 this occurs at approximately q_L = 19°.

The vision algorithm has been applied to a wide variety of images under different wheel slip and terrain unevenness conditions. Terrain types of various colors were tested, with and without rocks. Lighting was varied from uniform, diffuse illumination to a point-source which cast sharp shadows (see Figure 12).

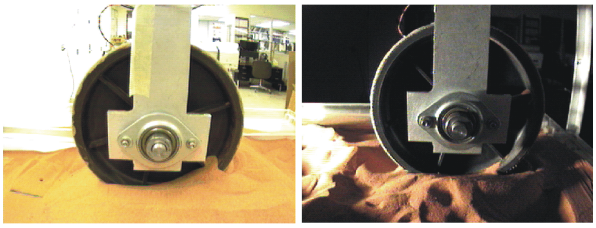

Figure 12. Sample wheel sinkage estimation images

Table 2 shows results from six image sets of 19 images each. Percent error is computed as the difference between the visually-estimated angle and the actual angle, as a fraction of the wheel radius, for the left- and right-hand angles. Image set 1 shows a wheel moving through flat bentonite clay under uniform lighting. Set 2 shows a wheel moving at very high slip ratio through flat JSC Mars-1 soil simulant under uniform lighting. Set 3 shows a wheel moving through uneven bentonite clay under uniform lighting. Set 4 shows a wheel moving through uneven, rocky bentonite clay under uniform lighting. Set 5 shows a stationary, sunken wheel in uneven bentonite illuminated by a moving point source. Set 6 shows a wheel moving through uneven bentonite illuminated by a stationary point source.

Table 2: Visual wheel sinkage estimation results

Image Set	Left-hand Angle RMS Error (%)	Right-hand Angle RMS Error (%)
1	1.08	1.61
2	2.40	2.46
3	2.33	2.48
4	5.21	2.06
5	5.10	12.10
6	8.85	14.01

Generally, the algorithm accurately detected the wheel sinkage under a wide range of conditions. Errors in set 4 were occasionally caused by rocks occluding the wheel-terrain interface. These errors

could be mitigated in the future by a texture- or geometry-based rock detection algorithm.

A more frequent error source was uneven lighting. Sets 5 and 6 evidence higher RMS error than sets 1-4. Reflections off the wheel rim occasionally caused misidentifications. Other problems were the result of shadows falling on uneven terrain itself. However, these errors tended to appear as easily-identifiable "outliers" (i.e. the errors appeared as large anomalous changes in the estimated angle). These errors could be mitigated by intelligent filtering. This is a current area of research.

Extension of the algorithm to multi-channel image data from a color camera was explored. Here, the wheel rim was colored blue, to aid differentiation between wheel and terrain. Techniques for exploiting color data included examining various distance metrics in RGB space from the known wheel color to the terrain color. All of these methods accurately identified the wheel/terrain interface in fully-lit conditions with uniform terrain. Several of them appeared to be more robust than the single-channel algorithm in rejecting errors caused by intervening rocks. However these techniques were equally likely to exhibit erroneous estimation under low light conditions with shadows. In general there appeared to be little advantage to employ color-based sinkage estimation over grayscale.

4. Conclusions and Future Work

This paper has presented methods for terrain estimation and sensing. A method for on-line terrain parameter estimation was presented and shown to be effective in simulation and experimental trials. A complementary method for terrain traversability estimation was also presented. A vision-based method for measuring wheel sinkage was described and shown to be accurate and relatively robust to lighting variation. It was shown that these techniques can be used to gain important information about a rover's surrounding terrain

Future work in these area will focus on using of visual cues to correlate local and distant terrain. Terrain-based motion planning will also be addressed.

Acknowledgements

This work is currently supported by the NASA Jet Propulsion Laboratory through the Mars Technology Program. The authors would like to acknowledge the support of Drs. Paul Schenker, Samad Hayati, and Rich Volpe.

References

[1] Bekker, G., *Introduction to Terrain-Vehicle Systems*, University of Michigan Press, 1969.

[2] Iagnemma, K., Genot, F. and Dubowsky, S., "Rapid Physics-based Rough-Terrain Rover Planning with Sensor and Control Uncertainty", *Proc. of the IEEE International conference on Robotics & Automation*, 1999.

[3] Iagnemma, K., and Dubowsky, S., "Mobile Robot Rough-Terrain Control (RTC) for Planetary Exploration," *Proceedings of the 26th ASME Biennial Mechanisms and Robotics Conference, DETC 2000*, 2000.

[4] Iagnemma, K., Shibly, H., and Dubowsky, S., "On-Line Terrain Parameter Estimation for Planetary Rovers," *Proc. of IEEE International Conference on Robotics and Automation*, 2002.

[5] Matijevic, J., et al., "Characterization of Martian Surface Deposits by the Mars Pathfinder Rover, Sojourner," *Science*, **278**, 5, 1997

[6] Nohse, Y. et al, "A Measurement of Basic Mechanical Quantities of Off-the-Road Traveling Performance", *Journal of Terramechanics,* **28**, No. 4 1991.

[7] Olson, C., Matthies, L., Schoppers, M., and Maimone, M., "Stereo Ego-motion Improvements for Robust Rover Navigation," *Proc. of IEEE International Conference on Robotics and Automation*, 2001.

[8] Volpe, R., "Rover Functional Autonomy Development for the Mars Mobile Science Laboratory," *Proc. of 2003 IEEE Aerospace Conference*, 2003

[9] Wong, J. and Reece, A., "Prediction of Rigid Wheel Performance Based on the Analysis of Soil-Wheel Stresses Part 1", *Journal of Terramechanics*, **4**, 1, 1976.

[10] Wong, J, *Theory of Ground Vehicles*, Wiley, 2001.